catalysts

MDPI

Article

Two-Step Dry Gel Method Produces MgAPO-11 with Low Aspect Ratio and Improved Catalytic Performance in the Conversion of Methanol to Hydrocarbons

Lina Zhang [1,2], Daniel Sean Firth [1], Unni Olsbye [1,*] and Xiaojun Bao [3]

[1] Center for Materials Science and Nanotechnology, Department of Chemistry, University of Oslo, P.O. Box 1033 Blindern, N-0315 Oslo, Norway; upczhlina@163.com (L.Z.); danielfirth.mail@gmail.com (D.S.F.)
[2] Sinopec Beijing Research Institute of Chemical Industry, Beijing 100728, China
[3] National Engineering Research Center of Chemical Fertilizer, College of Chemical Engineering, Fuzhou University, Fuzhou 350116, China; baoxj@fzu.edu.cn
* Correspondence: unni.olsbye@kjemi.uio.no; Tel.: +47-22-85-54-56

Abstract: In this article, the synthesis, characterization and catalytic performance of three MgAPO-11 catalysts with distinct crystal morphologies (sunflower, ball and candy) are presented. Among the three samples, the candy-like MgAPO-11-C, with high crystallinity and uniform particle size (of about 1 μm), was synthesized for the first time by using a unique two-step dry gel method. Despite the similar acid strength of the three samples, the different and distinct morphologies of the catalysts resulted in very different methanol-to-hydrocarbons (MTH) performances. In particular, the candy-like MgAPO-11-C presented the best MTH performance with the highest total conversion capacity (4.4 $g_{MeOH} \cdot g_{catalyst}^{-1}$ h^{-1}) and the best selectivity to C_{5+} aliphatics (64%).

Keywords: MgAPO-11; methanol to hydrocarbons; dry gel method; crystal morphology; candy like

check for updates

Citation: Zhang, L.; Firth, D.S.; Olsbye, U.; Bao, X. Two-Step Dry Gel Method Produces MgAPO-11 with Low Aspect Ratio and Improved Catalytic Performance in the Conversion of Methanol to Hydrocarbons. *Catalysts* **2022**, *12*, 413. https://doi.org/10.3390/catal12040413

Academic Editors: John Vakros, Giuseppe Bonura, Catia Cannilla and Evroula Hapeshi

Received: 11 February 2022
Accepted: 31 March 2022
Published: 7 April 2022

Publisher's Note: MDPI stays neutral with regard to jurisdictional claims in published maps and institutional affiliations.

Copyright: © 2022 by the authors. Licensee MDPI, Basel, Switzerland. This article is an open access article distributed under the terms and conditions of the Creative Commons Attribution (CC BY) license (https://creativecommons.org/licenses/by/4.0/).

1. Introduction

Despite decreasing crude oil reservoirs and pressing environmental concerns, the global demand for energy and petrochemical products is still increasing [1–3]. This situation calls for alternative routes for the manufacture of such products [4–6]. The conversion of renewable and recycled C/H sources into high-value products is considered a promising path towards meeting this increasing demand. The methanol-to-hydrocarbons (MTH) reaction is the final step in such a process [7]. Zeolites and zeotypes, known as shape selective materials, are key for the MTH reaction, due to their ability to distinguish between reactants, products and reaction intermediates, based on their molecular size. Mechanistic studies indicate that the MTH reaction proceeds by a "hydrocarbon pool mechanism" as proposed by Dahl and Kolboe and built upon by Svelle et al. in the "dual cycle" mechanism [8,9]. The "Hydrocarbon pool mechanism" can be divided into two parts: one is the "alkene cycle" and the other is the "aromatic cycle". Ethene is produced primarily from the "aromatic cycle", while propene and higher alkenes may be formed from both cycles. This is due to the promotion of distinct reaction intermediates and reactions by each topology [7,10,11]. Furthermore, diffusion restrictions contribute substantially to product sieving into the bulk phase. Hence, the product distribution from a given feedstock may be tuned by using catalysts with different topology, such as the conversion of methanol to gasoline over ZSM-5 and methanol to olefins over SAPO-34 [12,13].

Recently, focus has been set on developing new molecular sieves for the MTH reaction, such as the one-dimensional zeolites ZSM-22 and ZSM-23 [14–17]. ZSM-22 and ZSM-23 contain one-dimensional non-intersecting 10-ring channels with diameters of 0.46 nm × 0.57 nm [15,18]. As a result of this unique channel structure, the "aromatic cycle" of the MTH reaction is highly restricted, and both ZSM-22 and ZSM-23 show a high

selectivity for C_5-C_{6+} alkenes, free of aromatics [17]. Hence, ZSM-22 and ZSM-23 based MTH products might help meet current and future petrochemical demands and could be suitable for gasoline production via hydrogenation. The 1D 10-ring zeolites are prone to rapid deactivation by the formation of aromatic compounds that block the access to pores containing the active sites [18]. Recent research demonstrated that a smaller particle size, characterized by a low aspect ratio, dramatically enhances the catalytic lifetime of ZSM-23 [15].

In another line of work, studies of the 1D 12-ring AFI structure showed that the addition of the isostructural AlPO-5 to a SSZ-24 zeolite increased its MTH turn-over number by facilitating methanol dehydration to dimethyl ether (DME) [19]. Furthermore, studies of MAPO-5 (M = Mg, Co, Zn, Si, Ti, Zr) suggested that the more strongly acidic MgAPO-5 analogue favors the alkene cycle over the arene cycle compared to SAPO-5, leading to enhanced propene selectivity over MgAPO-5 [20,21]. Encouraged by these results, we decided to explore a 1D 10-ring MgAPO material, MgAPO-11, as a catalyst for the MTH reaction.

The zeotype $AlPO_4$-11 material has an AEL topology and consists of alternating, $(AlO_4)^-$ and $(PO_4)^+$ tetrahedra, resulting in a neutral framework [22–24]. In MgAPO-11, Al is partially substituted by Mg in the $AlPO_4$-11 lattice, thereby introducing Brønsted (B) acid sites [25,26]. The diameters of the major and minor axes of the 10-ring channels in MgAPO-11 are 0.65 nm and 0.43 nm. MgAPO-11 has attracted a great deal of attention due to its excellent performance in the hydroisomerization of n-alkanes, which produces low freezing point diesel, high octane number gasoline, and high viscosity lubricants [27–29]. However, to the best of our knowledge, the potential of MgAPO-11 as a catalyst for the MTH reaction is yet to be explored. Furthermore, most of the papers on MgAPO-11 have focused on MgAPO-11 with a large particle size along the single channel structure, which is less suitable for the MTH reaction [25,26,30]. Recently, Shu et al. successfully synthesized hierarchical MgAPO-11 molecular sieves by using the epoxide-mediated sol-gel method, however, the synthesis uses propylene oxide and harsh conditions (ice-cooled conditions) [27]. Searching for a simpler synthesis procedure to obtain small, hierarchical MgAPO-11 crystals, we found inspiration in two contributions from the Chen and Rimer groups, respectively, who used ethanol as a growth modifier to obtain zeolite L with a low aspect ratio [31,32].

In this work, a unique two-step dry gel method, using ethanol as a growth modifier, has been developed to synthesize MgAPO-11 with a low aspect ratio and hierarchical structure. The physical characteristics and catalytic properties of this material for the MTH process was compared to materials obtained by alternative synthesis routes. The effect of crystal morphology on the catalyst lifetime was profound. The best catalyst synthesized by the unique two-step dry gel method showed a conversion capacity seven-fold higher than the other samples that were synthesized.

2. Results and Discussion

2.1. Characterization

Scanning electron microscope (SEM) images (Figures 1 and S1) of the three MgAPO-11 samples clearly show three distinct morphologies (and particle sizes) produced by the three different synthesis methods used. These MgAPO-11 samples exhibited crystal morphologies reminiscent of sunflowers (MgAPO-11-S), balls (MgAPO-11-B), and candy (MgAPO-11-C). Close inspection of the SEM images reveals that MgAPO-11-S and MgAPO-11-B particles consist of bundles of needle-like crystals with a high aspect ratio. The MgAPO-11-S sunflowers are composed of approximately 5 μm long needles, while the MgAPO-11-B balls consist of approximately 2 μm long needle-like particles and some amorphous particles. In contrast, the 1 μm particles of MgAPO-11-C consisted of singular crystals with uneven surfaces and an aspect ratio close to unity. The elemental ratios of Mg and Al (Mg/Al) were calculated from scanning electron microscope-X-ray energy dispersion spectra (SEM-EDS)

(Table 1). The Mg/Al ratio of the three samples varied from 0.06 to 0.08, corresponding to the 305–399 µmol Mg/g sample.

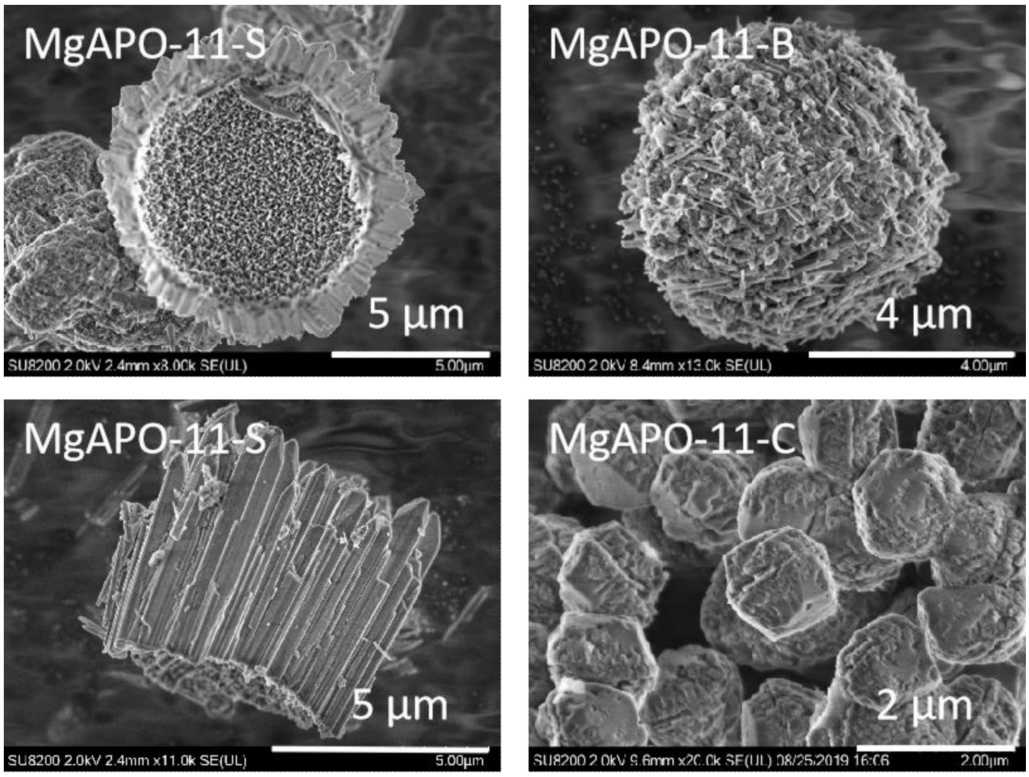

Figure 1. SEM images of the three MgAPO-11 samples.

Table 1. Acid amount and distribution of the acid sites of the MgAPO-11 samples.

Sample	Amount (µmol g^{-1}) and Distribution of Acid Sites [a]						Mg/Al Mol Ratio (SEM-EDX)
	Total Acid Sites (200 °C)			Strong Acid Sites (350 °C)			
	B	L	B + L	B	L	B + L	
MgAPO-11-S	16	44	60	7	22	29	0.06
MgAPO-11-B	8	54	62	1	20	21	0.07
MgAPO-11-C	31	76	107	9	67	76	0.08

[a] Calculated from the Py-IR spectra.

Powder X-ray Diffraction (PXRD) patterns of the three MgAPO-11 samples (Figure 2a) were consistent with the AEL structure. MgAPO-11-B showed a lower peak intensity compared to the other two samples, probably due to the existence of an amorphous phase [33]. MgAPO-11-C displayed the highest peak intensity among the three samples, indicating that it had the highest crystallinity [34].

The local atomic environment of P in the three MgAPO-11 samples was investigated using solid-state NMR analysis. The ^{31}P magic angle spinning nuclear magnetic resonance (^{31}P MAS NMR) spectrum (Figure 2b) of all three samples exhibited an intense peak at −30 ppm and a shoulder peak at −24 ppm, and we have attributed this to the tetrahedral P(4Al) environment and P(3Al, 1Mg), respectively [27,35]. In addition, there is a broad peak at 0 to −20 ppm for MgAPO-11-B, and this broad peak may be assigned for P(2Al, 2Mg) and P(1Al, 3Mg) [36]. These results further confirmed the successful introduction of Mg^{2+} into the framework.

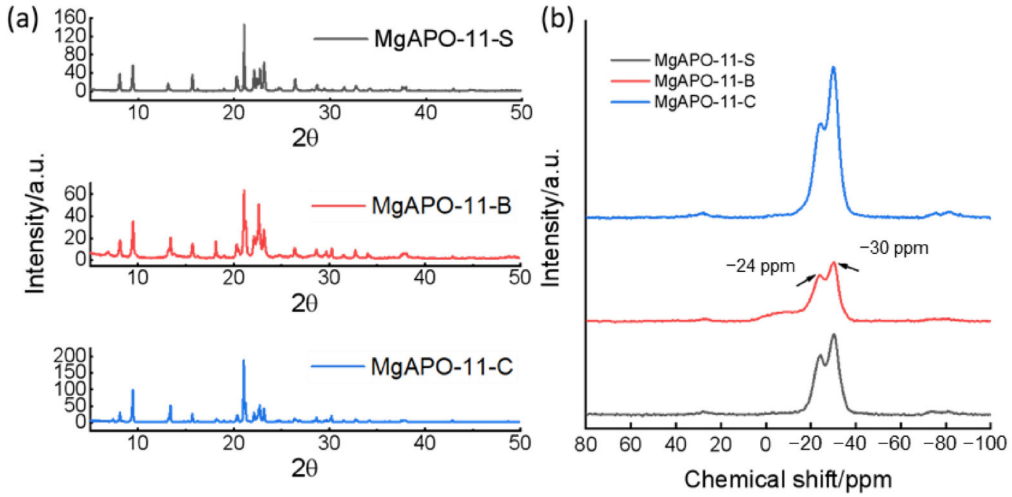

Figure 2. PXRD and MAS NMR data for MgAPO-11 Samples (**a**) PXRD patterns and (**b**) ^{31}P MAS NMR of the three MgAPO-11 samples.

The acid strength of the three MgAPO-11 samples was characterized by the temperature programmed desorption of ammonia (NH_3-TPD). All three MgAPO-11 samples displayed similar peak centers indicating a similar distribution of sites with weak and strong acid strength among all samples (Figure 3a). The nature and concentration of acid sites present in the three MgAPO-11 samples were investigated by pyridine infrared (Py-IR) characterization (Figure 3b). The two bands at 1540 and 1450 cm^{-1} are assigned to pyridine adsorbed on Brønsted (B) and Lewis (L) acid sites, respectively. The total number of acid sites and strong acid sites were measured by Py-IR at 200 and 350 °C, respectively (Table 1). These results showed that, among all three MgAPO-11 samples, MgAPO-11C had the largest number of weak and strong B and L acid sites accessible for pyridine. The low number of B sites available to pyridine compared to the total amount of Mg in the samples could be linked to extra-framework Mg, as well as to restricted diffusion of pyridine into the crystals. Since the size of pyridine is close to the size of the AEL pores, the latter effect is probably important. The difference in acid strength distribution between ammonia adsorption and pyridine adsorption (Figure 3, Table 1) points in this direction.

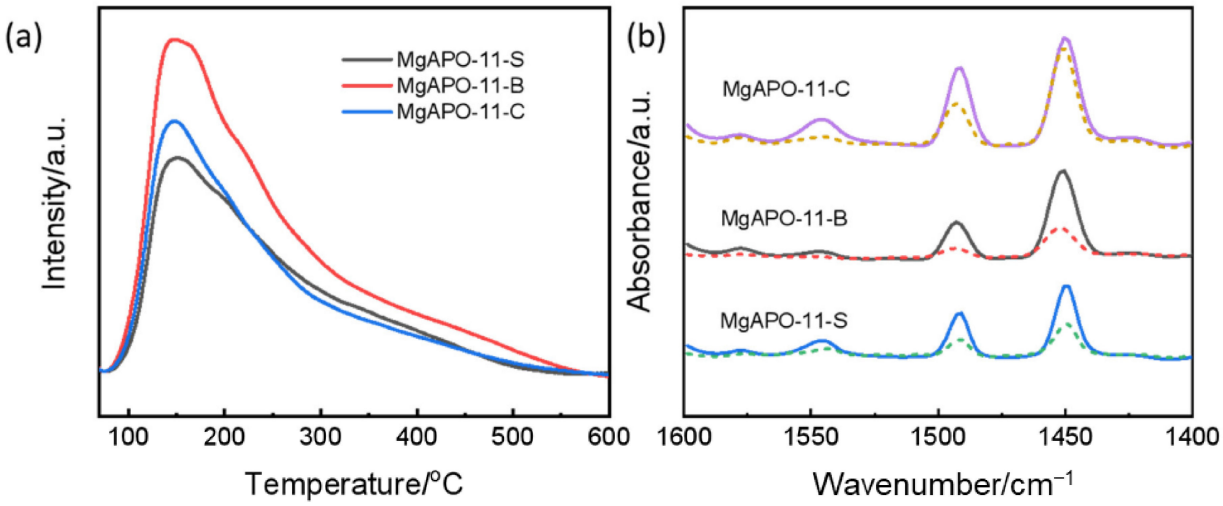

Figure 3. Characterization data of the amount and strength of acid sites in all MgAPO-11 samples: (**a**) NH_3-TPD profiles and (**b**) Py-IR spectra of the three MgAPO-11 samples at 200 (solid line) and 350 °C (dotted line).

The N_2 adsorption-desorption isotherms (Figure S2A) for MgAPO-11-C exhibited behavior typical for a type-IV isotherm with a H4 type hysteresis loop. This is indicative of a material with uniform slit-like mesopores. In comparison, MgAPO-11-B and MgAPO-11-S exhibited a type-IV isotherm with a H3 type hysteresis loop behavior, indicating an uneven distribution of slit-like mesopores, as confirmed by pore size distribution plots (Figure S2B) [37]. Hence, micropores and mesopores co-exist in all three samples [38].

The textural properties of the three MgAPO-11 samples are listed in Table 2 and highlights the advantageous properties of MgAPO-11-C that were achieved using this two-step dry gel method. MgAPO-11-C not only showed the largest Brunauer-Emmett-Teller (BET) surface area (254 $m^2 \cdot g^{-1}$) compared with MgAPO-11-S (95 $m^2 \cdot g^{-1}$) and MgAPO-11-B (187 $m^2 \cdot g^{-1}$). It was also shown to be larger than that achieved previously for MgAPO-11 (175 $m^2 \cdot g^{-1}$) synthesized by a traditional dry-gel method [27]. In addition, MgAPO-11-C showed the highest external specific surface area (177 $m^2 \cdot g^{-1}$) and highest hierarchical factor (0.093) of all three samples. This indicates that this two-step dry gel method is able to produce small and highly mesoporous MgAPO-11 particles not seen with the traditional dry-gel methods and the other two methods reported in this work. The micropore volume of the MgAPO-11-C (0.037 $m^3 \cdot g^{-1}$) was much larger than that of MgAPO-11-S (0.018 $m^3 \cdot g^{-1}$) and MgAPO-11-B (0.018 $m^3 \cdot g^{-1}$), yet smaller than MgAPO-11 synthesized by traditional dry-gel method (0.06 $m^3 \cdot g^{-1}$) [27]. This result indicates that the dry-gel method is beneficial for the synthesis of a mesoporous MgAPO-11, without the loss of the microporous structure.

Table 2. Characterization data of the MgAPO-11 samples.

Sample	MgAPO-11-S	MgAPO-11-B	MgAPO-11-C
S_{BET} [a] ($m^2 \cdot g^{-1}$)	95	187	254
S_{mic} ($m^2 \cdot g^{-1}$)	43	39	77
S_{ext} ($m^2 \cdot g^{-1}$)	52	148	177
V_{Total} [b] ($m^3 \cdot g^{-1}$)	0.147	0.464	0.276
V_{mic} [c] ($m^3 \cdot g^{-1}$)	0.018	0.018	0.037
V_{meso} [d] ($m^3 \cdot g^{-1}$)	0.129	0.446	0.239
Hierarchy factor [e]	0.067	0.031	0.093
Conversion capacity ($g_{MeOH} \cdot g_{cat}^{-1}$)	0.7	0.6	4.4
Coke content [f] (%, $g \cdot g_{cat}^{-1}$)	3.14	4.79	7.22
R_{coke} [g] ($mg \cdot min^{-1}$)	0.733	1.362	0.584

[a] Brunauer–Emmett–Teller (BET) surface area; [b] Total pore volume at $P/P_0 = 0.990$; [c] Micropore volume from *t*-plot; [d] $V_{meso} = V_{Total} - V_{mic}$; [e] Hierarchy factor = $(V_{mic}/V_{Total}) \times (S_{ext}/S_{BET})$; [f] The content of coke was analyzed by Thermo-gravimetric (TG) up to 800 °C with a ramp rate of 10 °C/min; [g] R_{coke} = coke amount/reaction time.

2.2. Catalytic Activity

The catalytic performance tests of the three MgAPO-11 catalysts were carried out at atmospheric pressure and 450 °C, with a weight hourly space velocity (WHSV) of $0.5 \cdot h^{-1}$ (Figure 4). The three catalysts displayed a wide variation in lifetime (Figure 4a). This is quantified further by comparing the total conversion capacities (Table 2), defined as the total amount of methanol converted into hydrocarbons until complete deactivation [17]. MgAPO-11-C showed the highest total conversion capacity of all three samples with 4.4 $g_{MeOH} \cdot g_{cat}^{-1}$, six- to seven-fold larger than MgAPO-11-S and MgAPO-11-B, respectively (Table 2). In addition to morphology and crystal size, the total conversion capacity also varied with the Mg content of the catalysts. For MgAPO-11-C samples synthesized with an increasing Mg content (Figures S3–S8), the total conversion capacity also increased from 0.2 to 4.4 $g_{MeOH} \cdot g_{cat}^{-1}$. With the exception of MgAPO-11-S, a linear relationship was observed between the amount of Brønsted acid sites accessible to pyridine and the total conversion capacity of each sample (Figure S9). All tested MgAPO-11 samples displayed a similar slope in their deactivation curves, which was typically seen when the methanol conversion had dropped to 80%. At this stage, the activity drop was close to 20 conversion points per hour. Overall, the test results and characterization data suggest that the main reason for the difference in conversion capacity is the number of accessible B

acid sites (Tables 1 and S1, Figure S9). A similar conclusion has previously been reached for zeolites with ZSM-22 and ZSM-23 topologies [15,16,39]. In order to further explore the deactivation process of the three catalysts, the amount of the deposited coke of the three deactivated samples was analyzed after the MTH reaction. The weight losses for MgAPO-11-S, MgAPO-11-B and MgAPO-11-C were 3.74%, 4.79% and 7.22%, respectively (Table 2 and Figures S10 and S11), which are obtained by burning the retained coke species. Considering the different reaction times for the three catalysts, the average coke formation rate was calculated by using the equation: R_{coke} = coke amount/reaction time. The R_{coke} value of MgAPO-11-C (0.584) is much lower than that of MgAPO-11-S (0.733) and MgAPO-11-B (1.362), which agrees with the better performance and longer lifetime of MgAPO-11-C.

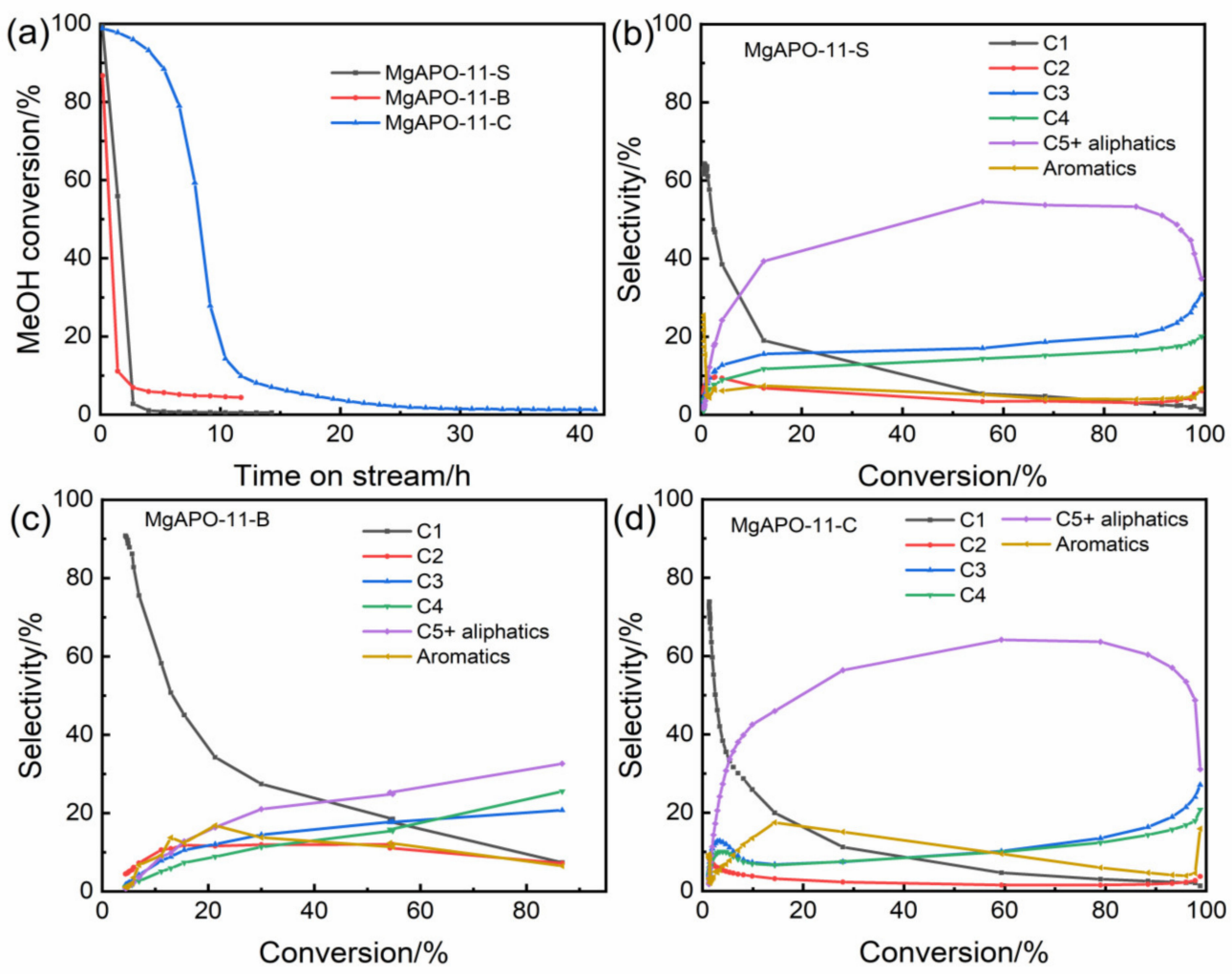

Figure 4. MTH performance of three MgAPO-11 catalysts at 450 °C and WHSV = 0.5 h^{-1}. The data were obtained during catalyst deactivation: (**a**) MeOH conversion versus time on stream for all three MgAPO-11 samples, (**b**) conversion versus selectivity performance of MgAPO-11-S, (**c**) conversion versus selectivity performance of MgAPO-11-B, (**d**) conversion versus selectivity performance of MgAPO-11-C.

Considering next the product selectivity of the MgAPO-11 samples, C_{5+} aliphatics was the main product obtained over all samples (Figure 4b–d). Focusing first on MgAPO-11-C, it displayed a selectivity pattern where: C_{5+} >> C_3 > C_4 >> C_2 > C_1. The maximum C_{5+} selectivity obtained was 64%. With progressive deactivation, the aromatics selectivity rose to become the second most abundant product, followed by methane (C_1). Considering the small pore size of MgAPO-11, it is likely that aromatic products were formed either at the

micropore pore mouth, in the mesopores or at the external surface of MgAPO-11-C. Focusing next on MgAPO-11-S, its selectivity pattern was very similar to that of MgAPO-11-C, although with somewhat higher selectivity to C_2–C_4, giving a maximum C_{5+} aliphatics selectivity of 55 %. Considering, finally, MgAPO-11-B, C_{5+} aliphatics was still the main product (maximum 33% selectivity), yet with even higher selectivity towards C_2-C_4, and to methane and aromatics with progressive deactivation, compared to the other two samples. To elaborate on the selectivity variations, it is necessary to turn to the MTH reaction scheme, as described in a recent review [1]. Methane, ethene and propene are primary products of the initiation reactions leading to the first C-C bond formation. During steady-state hydrocarbon pool operation, propene and butenes are formed from the cracking of higher hydrocarbons, and from ethene/propene methylation. Ethene is mainly formed from dealkylation of polymethylated benzene (and naphthalene) intermediates. Considering the prior work on 1D 10-ring zeolites (ZSM-22, ZSM-23), aromatic products were found to be virtually inert to further reaction, and even the cracking of higher hydrocarbons is severely restricted by the small pore size [40,41]. With the similar pore size of MgAPO-11 and those zeolites, it is likely that cracking and dealkylation reactions are also restricted in MgAPO-11. Although we have no direct evidence, it is tempting to suggest that the higher selectivity to C_1-C_4 products in the MgAPO-11-B and MgAPO-11-S materials may be due to a higher relative abundance of initiation reactions compared to hydrocarbon pool propagation reactions, in these materials compared to MgAPO-11-C. This suggestion would be in line with the lower conversion capacity observed for MgAPO-11-B and MgAPO-11-S.

The aim of this study was to explore the potential of MgAPO-11 as a catalyst for the MTH reaction. As already pointed out, this material has similar pore size and dimensionality to ZSM-22 and ZSM-23. Considering the product selectivity of MgAPO-11, it is also very similar to ZSM-22 and ZSM-23, with the aliphatics selectivity decreasing in the order: $C_{5+} >> C_3 > C_4 >> C_2 > C_1$. A direct comparison between the materials is complicated by the fact that ZSM-22 and ZSM-23 selectivity results are reported at 400 °C, while MgAPO-11 was tested at 450 °C. However, keeping in mind that the comparison is rather qualitative, the maximum C_{5+} aliphatics selectivity reported for ZSM-22 is around 70%, somewhat higher than the 64% maximum selectivity reported for MgAPO-11-C in this work. Furthermore, the maximum conversion capacity of ZSM-22 reported at 450 °C was 12 $g_{MeOH} \cdot g_{cat}{}^{-1}$ [39], 2.7 times that reported for MgAPO-11-C here. Considering the results reported in this work and the deactivation pattern of 1D 10-ring structures during the MTH reaction, the difference is probably strongly related to the contact time and number of accessible Brønsted acid sites in the two materials [18,39].

3. Materials and Methods

3.1. Materials

The reagents used include phosphoric acid (85% H_3PO_4), aluminum isopropoxide (≥98%), dipropylamine (DPA) (99%), tetraethyl orthosilicate (TEOS) (98%), cetyltrimethylammonium bromide (CTAB) (≥98%), Pluronic®-F127 (98%), $Mg(NO_3)_2 \cdot 6H_2O$ (99%), $Mg(OAc)_2 \cdot 4H_2O$ (≥98%), pseudoboehmite (Pural SB), and boehmite (Catapal B). All of the above chemicals were purchased from Sigma-Aldrich, except pseudoboehmite and boehmite, which were from Sasol. All chemicals and reagents were used without further purification. MgAPO-11 catalysts with different morphologies were prepared using initial gel compositions, as listed in Table 3. The methods are detailed below.

Table 3. Precursor gel molar batch compositions of the different samples of MgAPO-11.

Catalyst	Al_2O_3	P_2O_5	MgO	DPA	H_2O	CTAB	F127	EtOH	Al Source	Mg Source
MAPO-11-S	1	1	0.1	1.5	40	-	-	-	Boehmite	$Mg(NO_3)_2 \cdot 6H_2O$
MAPO-11-B	1	0.74	0.1	0.93	41	0.03	0.001	-	Pseudoboehmite	$Mg(OAc)_2 \cdot 4H_2O$
MAPO-11-C	1	1	0.1	1.5	50	-	-	64.5	Aluminium isopropoxide	$Mg(OAc)_2 \cdot 4H2O$

3.1.1. Synthesis of MgAPO-11-S

For the synthesis of MgAPO-11-S, 3.0 g of boehmite was dissolved in 16.0 g of deionized water and stirred for 1 h at 25 °C. Then 5.1 g of H_3PO_4 was added, followed by the addition of 0.6 g of $Mg(NO_3)_2{\cdot}6H_2O$ and stirring at 25 °C. After 4 h, 3.4 g of di-n-propylamine (DPA) was added and the gel stirred for another 24 h at 25 °C. Finally, the gel was transferred into a 45 mL PTFE-lined stainless-steel autoclave and pre-crystalized at 100 °C for 24 h with rotation (25 rpm), followed by crystallization at 200 °C for an additional 24 h with rotation (25 rpm). The resultant solid was recovered by filtration, washed three times with deionized water and dried at 100 °C. The template was subsequently removed by calcination at 600 °C for 4 h in air.

3.1.2. Synthesis of MgAPO-11-B

MgAPO-11-B was synthesized based on the two-stage hydrothermal crystallization method previously reported by Zhang et al. with Mg replacing Si in the synthesis [42]. In detail, the first stage involves the addition of 4.2 g of H_3PO_4, 3.5 g of pseudoboehmite and 2.4 g of di-n-propylamine (DPA) template to a beaker containing 17.7 g deionized water under stirring at 25 °C. After 24 h of stirring at 25 °C, the gel was transferred to a PTFE-lined stainless-steel autoclave and pre-crystallized at 150 °C for 6 h with rotation (25 rpm). For the second stage, 0.27 g of CTAB, 0.31 g of F127 and 0.54 g of $Mg(OAc)_2{\cdot}4H_2O$ were added to the precursor gel, stirred for 4 h at 25 °C and then crystallized at 185 °C for another 24 h with rotation (25 rpm). The resultant solid was recovered by filtration, then washed three times with water and dried at 100 °C. The template was subsequently removed by calcination at 600 °C for 4 h in air.

3.1.3. Synthesis of MgAPO-11-C

MgAPO-11-C was synthesized using a two-step dry gel method. Then, 5.0 g of $Al(O\text{-}i\text{-}Pr)_3$ and 2.8 g of H_3PO_4 were dissolved in 8.5 g of deionized water and stirred for 4 h at 25 °C. This was followed by adding 0.26 g of $Mg(NO_3)_2{\cdot}6H_2O$ and 2.5 g of DPA under stirring at 25 °C. The gel was then transferred into a 45 mL PTFE-lined stainless-steel autoclave and pre-crystalized at 160 °C for 24 h with rotation (25 rpm). After 24 h, the gel was placed in a 60 °C oil bath and the solvent evaporated. Once evaporated, 25 mL of ethanol was added and the mixture gel stirred for 6 h at 60 °C. Finally, the gel was transferred into a 45 mL PTFE-lined stainless-steel autoclave and crystallized at 200 °C for 24 h. The resultant solid was recovered by filtration, which was washed three times with ethanol and dried at 100 °C. The template was subsequently removed by calcination at 600 °C for 4 h in air.

The unique point of the current synthesis method compared to those used in the prior literature is that a two-step dry gel method with additional controlled solvent evaporation was used to achieve the small and hierarchical MgAPO-11 particles. Control of the solvent evaporation process is important; as ethanol needs to be evaporated, although only to an extent where some ethanol is left for the second step crystallization to work. When ethanol was replaced with water, larger crystals with a high aspect ratio were obtained.

3.2. Catalyst Characterization

Siemens Bruker D500 in Graff Brentano geometry with Cu Kα radiation (λ = 1.5406 Å) was used to conduct the PXRD measurements. The size and morphology of samples were evaluated by using a Hitachi SU 8230 field-emission environmental scanning electron microscope (FESEM). The textural properties of the calcined samples were tested by N_2 adsorption-desorption measurements at −196 °C (Belsorp-mini II). The specific surface areas of the samples were analyzed by the BET method and the surface areas and pore volumes of the samples were calculated by the t-plot method. The strength and distribution of acid sites were analyzed by NH_3-TPD. Py-IR adsorption spectra were obtained on a Nicolet 5700 spectrometer with a resolution of 1 cm^{-1}. ^{31}P MAS NMR spectroscopy characterization was carried out on a Bruker DSX 500 MHz NMR spectrometer. TG analyses

were performed on a Mettler Toledo instrument, in which each sample was heated between 40 and 800 °C at a ramp rate of 10 °C/min in an air flow.

3.3. Catalytic Testing

The MTO performance testing of the samples was performed in a continuous down-flow bed U-shaped quartz reactor (4 mm in internal diameter). The test rig was equipped with Brooks mass flow controllers for gas feeding at atmospheric pressure. Then, 0.2 g of a calcined MgAPO-11 catalyst was loaded into the reactor and pre-treated in a pure O_2 flow of 25 mL/min at 550 °C for 2 h before each run. The reactor was subsequently cooled down to 450 °C in an He flow. Methanol was fed to the reactor by bubbling an He flow (3.3 mL/min) through a methanol saturator. The saturator temperature was kept at 35 °C, giving rise to a methanol partial pressure of 280 mbar, corresponding to a methanol flow of 1.3 mL/min and a WHSV of 0.5 h^{-1}. The reaction products were analyzed using an online gas chromatograph (Agilent 6890 A) with a flame ionization detector (FID) and a capillary Rtx-DHA-150 column (60 m × 0.53 mm × 3 μm).

4. Conclusions

Three MgAPO-11 samples with different morphologies were successfully synthesized, including a candy-like MgAPO-11-C with a low aspect ratio obtained by using a novel two-step dry gel method. The three MgAPO-11 samples had similar acid strength distribution, however, they had dramatically different crystal morphologies and number of accessible Brønsted acid sites. The catalytic performance of the three MgAPO-11 materials for the MTH reaction was evaluated at 450 °C. The candy-like MgAPO-11-C with its smaller particle size and higher number of accessible Brønsted acid sites showed the highest stability and selectivity to C_{5+} aliphatics.

In summary, it is demonstrated that the size and shape of MgAPO-11 particles can heavily influence their stability and selectivity to C_{5+} aliphatics in the MTH process. This article also presents a novel route to prepare MgAPO-11 catalysts.

Supplementary Materials: The following supporting information can be downloaded at: https://www.mdpi.com/article/10.3390/catal12040413/s1, Table S1: Amount and distribution of acid sites in MgAPO-11 with different Mg contents; Figure S1: SEM images of the three MgAPO-11 samples with distinct morphologies; Figure S2: Nitrogen adsorption-desorption isotherms of the three MgAPO-11 samples with distinct morphologies; Figure S3: SEM images of MgAPO-11-C samples with different Mg contents; Figure S4: XRD patterns of the MgAPO-11-C samples with different Mg contents; Figure S5: NH_3-TPD profiles of the MgAPO-11-C samples with different Mg contents; Figure S6: Py-IR spectra of MgAPO-11 with different Mg contents; Figure S7: N_2 adsorption and desorption isotherms of the MgAPO-11-C samples with different Mg contents; Figure S8: Methanol conversion as a function of time on stream of the MgAPO-11-C samples with different Mg contents; Figure S9: Methanol conversion capacity versus accessible Brønsted acid sites; Figure S10: TG curves of the three MgAPO-11 samples with distinct morphologies after reaction; Figure S11: Photos of the three MgAPO-11 samples after reaction.

Author Contributions: Writing—original draft preparation, L.Z.; writing—review and editing, L.Z., D.S.F., U.O. and X.B.; supervision, U.O.; project administration, U.O. All authors have read and agreed to the published version of the manuscript.

Funding: This research was funded by the Norwegian Research Council, grant number 288331 (CO2LO) and EU framework Programme for Research and Innovation Horizon 2020 project BiZeolCat, grant agreement 814671.

Data Availability Statement: Not applicable.

Acknowledgments: This work was supported by the China Scholarship Council and Center for Materials Science and Nanotechnology of University of Oslo.

Conflicts of Interest: The authors declare no conflict of interest.

References

1. Yarulina, I.; Chowdhury, A.D.; Meirer, F.; Weckhuysen, B.M.; Gascon, J. Recent trends and fundamental insights in the methanol-to-hydrocarbons process. *Nat. Catal.* **2018**, *1*, 398–411. [CrossRef]
2. Sun, Q.; Yu, J.; Xie, Z. The state-of-the-art synthetic strategies for SAPO-34 zeolite catalysts in methanol-to-olefin conversion. *Natl. Sci. Rev.* **2017**, *5*, 542–558. [CrossRef]
3. Lefevere, J.; Mullens, S.; Meynen, V.; Noyen, J. Structured catalysts for methanol-to-olefins conversion: A review. *Chem. Pap.* **2014**, *68*, 1143–1153. [CrossRef]
4. Jia, Y.; Wang, J.; Zhang, K.; Feng, W.; Liu, S.; Ding, C.; Liu, P. Nanocrystallite self-assembled hierarchical ZSM-5 zeolite microsphere for methanol to aromatics. *Microporous Mesoporous Mater.* **2017**, *247*, 103–115. [CrossRef]
5. Zhou, F.; Gao, Y.; Wu, G.; Ma, F.; Liu, C. Improved catalytic performance and decreased coke formation in post-treated ZSM-5 zeolites for methanol aromatization. *Microporous Mesoporous Mater.* **2017**, *240*, 96–107. [CrossRef]
6. Wang, X.; Wen, M.; Wang, C.; Ding, J.; Sun, Y.; Liu, Y.; Lu, Y. Microstructured fiber@HZSM-5 core-shell catalysts with dramatic selectivity and stability improvement for the methanol-to-propylene process. *Chem. Commun.* **2014**, *50*, 6343–6345. [CrossRef]
7. Olsbye, U.; Svelle, S.; Bjørgen, M.; Beato, P.; Janssens, T.V.W.; Joensen, F.; Bordiga, S.; Lillerud, K.P. Conversion of methanol to hydrocarbons: How zeolite cavity and pore size controls product selectivity. *Angew. Chem. Int. Ed.* **2012**, *51*, 5810–5831. [CrossRef]
8. Stöcker, M. Methanol-to-hydrocarbons catalytic materials and their behavior. *Microporous Mesoporous Mater.* **1999**, *29*, 3–48. [CrossRef]
9. Bjorgen, M.; Svelle, S.; Joensen, F.; Nerlov, J.; Kolboe, S.; Bonino, F.; Palumbo, L.; Bordiga, S.; Olsbye, U. Conversion of methanol to hydrocarbons over zeolite H-ZSM-5: On the origin of the olefinic species. *J. Catal.* **2007**, *249*, 195–207. [CrossRef]
10. Ilias, S.; Bhan, A. Mechanism of the catalytic conversion of methanol to hydrocarbons. *ACS Catal.* **2013**, *3*, 18–31. [CrossRef]
11. Teketel, S.; Lundegaard, L.F.; Skistad, W.; Chavan, S.M.; Olsbye, U.; Lillerud, K.P.; Beato, P.; Svelle, S. Morphology-induced shape selectivity in zeolite catalysis. *J. Catal.* **2015**, *327*, 22–32. [CrossRef]
12. Zhang, S.; Gong, Y.; Zhang, L.; Liu, Y.; Dou, T.; Xu, J.; Deng, F. Hydrothermal treatment on ZSM-5 extrudates catalyst for methanol to propylene reaction: Finely tuning the acidic property. *Fuel Process. Technol.* **2015**, *129*, 130–138. [CrossRef]
13. Wang, C.; Xu, J.; Qi, G.; Gong, Y.; Wang, W.; Gao, P.; Wang, Q.; Feng, N.; Liu, X.; Deng, F. Methylbenzene hydrocarbon pool in methanol-to-olefins conversion over zeolite H-ZSM-5. *J. Catal.* **2015**, *332*, 127–137. [CrossRef]
14. Teketel, S.; Olsbye, U.; Lillerud, K.P.; Beato, P.; Svelle, S. Co-conversion of methanol and light alkenes over acidic zeolite catalyst H-ZSM-22: Simulated recycle of non-gasoline range products. *Appl. Catal. A Gen.* **2015**, *494*, 68–76. [CrossRef]
15. Molino, A.; Łukaszuk, K.A.; Rojo-Gama, D.; Lillerud, K.P.; Olsbye, U.; Bordiga, S.; Svelle, S.; Beato, P. Conversion of methanol to hydrocarbons over zeolite ZSM-23 (MTT): Exceptional effects of particle size on catalyst lifetime. *Chem. Commun.* **2017**, *53*, 6816–6819. [CrossRef]
16. Del Campo, P.; Olsbye, U.; Lillerud, K.P.; Svelle, S.; Beato, P. Impact of post-synthetic treatments on unidirectional H-ZSM-22 zeolite catalyst: Towards improved clean MTG catalytic process. *Catal. Today* **2018**, *299*, 135–145. [CrossRef]
17. Teketel, S.; Skistad, W.; Benard, S.; Olsbye, U.; Lillerud, K.P.; Beato, P.; Svelle, S. Shape selectivity in the conversion of methanol to hydrocarbons: The catalytic performance of one-dimensional 10-ring zeolites: ZSM-22, ZSM-23, ZSM-48, and EU-1. *ACS Catal.* **2011**, *2*, 26–37. [CrossRef]
18. Del Campo, P.; Slawinski, W.A.; Henry, R.; Erichsen, M.W.; Svelle, S.; Beato, P.; Wragg, D.; Olsbye, U. Time- and space-resolved high energy operando X-ray diffraction for monitoring the methanol to hydrocarbons reaction over H-ZSM-22 zeolite catalyst in different conditions. *Surf. Sci.* **2016**, *648*, 141–149. [CrossRef]
19. Martinez-Espin, J.S.; Morten, M.; Janssens, T.V.W.; Svelle, S.; Beato, P.; Olsbye, U. New insights into catalyst deactivation and product distribution of zeolites in the methanol-to-hydrocarbons (MTH) reaction with methanol and dimethyl ether feeds. *Catal. Sci. Technol.* **2017**, *7*, 2700–2716. [CrossRef]
20. Mortén, M.; Mentel, Ł.; Lazzarini, A.; Pankin, I.A.; Lamberti, C.; Bordiga, S.; Crocellà, V.; Svelle, S.; Lillerud, K.P.; Olsbye, U. A Systematic Study of Isomorphically Substituted H-MAlPO-5 Materials for the Methanol-to-Hydrocarbons Reaction. *ChemPhysChem* **2018**, *19*, 484–495. [CrossRef]
21. Mortén, M.; Cordero-Lanzac, T.; Cnudde, P.; Redekop, E.A.; Svelle, S.; van Speybroeck, V.; Olsbye, U. Acidity effect on benzene methylation kinetics over substituted H-MeAlPO-5 catalysts. *J. Catal.* **2021**, *404*, 594–606. [CrossRef]
22. Araujo, A.S.; Fernandes, V.J.; Silva, A.O.S.; Diniz, J.G. Evaluation of the AlPO-11 crystallinity by thermogravimetry. *J. Therm. Anal. Calorim.* **1999**, *56*, 151–157. [CrossRef]
23. Zhu, G.; Qiu, S.; Gao, F.; Wu, G.; Wang, R.; Li, B.; Fang, Q.; Li, Y.; Gao, B.; Xu, X. Synthesis of aluminophosphate molecular sieve $AlPO_4$-11 nanocrystals. *Microporous Mesoporous Mater.* **2001**, *50*, 129–135. [CrossRef]
24. Eswaramoorthy, M.; Jebarathinam, N.J.; Ulagappan, N.; Krishnasamy, V. Chromium substituted AlPO-11: Synthesis, characterisation and its application in oxidation reactions. *Catal. Lett.* **1996**, *38*, 255–259. [CrossRef]
25. Li, J.-J.; Guo, Y.; Li, G.-D.; Chen, J.-S.; Li, C.-J.; Zou, Y.-C. Investigation into the role of MgO in the synthesis of MAPO-11 large single crystals. *Microporous Mesoporous Mater.* **2005**, *79*, 79–84. [CrossRef]
26. Yang, X.; Xu, Z.; Tian, Z.; Ma, H.; Xu, Y.; Qu, W.; Lin, L. Performance of Pt/MgAPO-11 catalysts in the hydroisomerization of n-dodecane. *Catal. Lett.* **2006**, *109*, 139–145. [CrossRef]
27. Tao, S.; Li, X.; Gong, H.; Jiang, Q.; Yu, W.; Ma, H.; Xu, R.; Tian, Z. Confined-space synthesis of hierarchical MgAPO-11 molecular sieves with good hydroisomerization performance. *Microporous Mesoporous Mater.* **2018**, *262*, 182–190. [CrossRef]

28. Liu, Y.X.; Lyu, Y.C.; Wang, B.J.; Wang, Y.; Liu, X.M.; Rood, M.J.; Liu, Z.; Yan, Z.F. Promoter effect of heteroatom substituted AlPO-11 molecular sieves in hydrocarbons cracking reaction. *J. Colloid Interf. Sci.* **2018**, *528*, 330–335. [CrossRef]
29. Feng, L.; Qi, X.; Li, Z.; Zhu, Y.; Li, X. Synthesis and characterization of magnesium-substituted aluminophosphate molecular sieves (MgAPO-11) and their kinetic study of catalytic cracking of n-Hexane. *Chin. J. Catal.* **2009**, *30*, 340–346. [CrossRef]
30. Yang, X.M.; Ma, H.J.; Xu, Z.S.; Xu, Y.P.; Tian, Z.J.; Lin, L.W. Hydroisomerization of n-dodecane over Pt/MeAPO-11 (Me = Mg, Mn, Co or Zn) catalysts. *Catal. Commun.* **2007**, *8*, 1232–1238. [CrossRef]
31. Gomez, A.G.; Silveira, G.d.; Doan, H.; Cheng, C.-H. A facile method to tune zeolite L crystals with low aspect ratio. *Chem. Commun.* **2011**, *47*, 5876–5878. [CrossRef] [PubMed]
32. Lupulescu, A.I.; Kumar, M.; Rimer, J.D. A Facile Strategy To Design Zeolite L Crystals with Tunable Morphology and Surface Architecture. *J. Am. Chem. Soc.* **2013**, *135*, 6608–6617. [CrossRef] [PubMed]
33. Zhang, P.; Liu, H.; Zhu, H.; Oyama, S.T.; Bao, X. Synthesis and catalytic application of alumina@SAPO-11 composite via the in situ assembly of silicoaluminophosphate nanoclusters at an alumina substrate. *Catal. Sci. Technol.* **2018**, *8*, 4209–4218. [CrossRef]
34. Zhu, J.; Cui, Y.; Wang, Y.; Wei, F. Direct synthesis of hierarchical zeolite from a natural layered material. *Chem. Commun.* **2009**, *22*, 3282–3284. [CrossRef]
35. Wang, L.; Xu, Y.P.; Wang, B.C.; Wang, S.J.; Yu, J.Y.; Tian, Z.J.; Lin, L.W. Ionothermal synthesis of magnesium-containing aluminophosphate molecular sieves and their catalytic performance. *Chem. Eur. J.* **2008**, *14*, 10551–10555. [CrossRef] [PubMed]
36. Deng, F.; Yue, Y.; Xiao, T.; Du, Y.; Ye, C.; An, L.; Wang, H. Substitution of aluminum in aluminophosphate molecular sieve by magnesium: A combined NMR and XRD study. *J. Phys. Chem.* **1995**, *99*, 6029–6035. [CrossRef]
37. Schmidt, F.; Paasch, S.; Brunner, E.; Kaskel, S. Carbon templated SAPO-34 with improved adsorption kinetics and catalytic performance in the MTO-reaction. *Microporous Mesoporous Mater.* **2012**, *164*, 214–221. [CrossRef]
38. Ding, J.; Liu, H.; Yuan, P.; Shi, G.; Bao, X. Catalytic properties of a hierarchical zeolite synthesized from a natural aluminosilicate mineral without the use of a secondary mesoscale template. *ChemCatChem* **2013**, *5*, 2258–2269. [CrossRef]
39. Teketel, S.; Svelle, S.; Lillerud, K.P.; Olsbye, U. Shape-selective conversion of methanol to hydrocarbons over 10-Ring unidirectional-channel acidic H-ZSM-22. *ChemCatChem* **2009**, *1*, 78–81. [CrossRef]
40. Teketel, S.; Olsbye, U.; Lillerud, K.-P.; Beato, P.; Svelle, S. Selectivity control through fundamental mechanistic insight in the conversion of methanol to hydrocarbons over zeolites. *Microporous Mesoporous Mater.* **2010**, *136*, 33–41. [CrossRef]
41. Teketel, S.; Westgård Erichsen, M.; Bleken, F.L.; Svelle, S.; Lillerud, K.P.; Olsbye, U. Shape selectivity in zeolite catalysis. In *The Methanol to Hydrocarbons (MTH) Reaction in J. Spivey*; Han, Y.-F., Dooley, K., Eds.; Royal Society of Chemistry: Cambridge, UK, 2014; Volume 26, pp. 179–217.
42. Zhang, P.; Liu, H.; Yue, Y.; Zhu, H.; Bao, X. Direct synthesis of hierarchical SAPO-11 molecular sieve with enhanced hydroisomerization performance. *Fuel Process. Technol.* **2018**, *179*, 72–85. [CrossRef]